Insensitivity of nucleation rate to order-disorder interfaces in reversible thermoelastic martensitic transformations

J. C. Lago, W. Cho, D. Salas, I. Karaman, and P. J. Shamberger

Department of Materials Science and Engineering, Texas A&M University, College Station, Texas 77843, USA

Reversible martensitic transformations nucleate from sparse defects that lower the transformation's nucleation energy barrier. However, most defects do not serve as potent nucleation sites and, instead, can pin boundary motion and impede phase growth. Identifying potent defects from the general defect population remains an open challenge and has important implications for engineering reversible alloys. This study considers the influence of mesoscale order-disorder domains and the phase boundaries between the $L2_1$ and $B2$ phases on nucleation kinetics. We use solution heat treatment and secondary annealing in $Ni_{45}Co_5Mn_{36.7}In_{13.3}$ microparticles to compare an average $L2_1$ domain interfacial area density of $590.6 - 50.6\,\mu m^{-1}$, measured from transmission electron microscopy micrographs using the intercept method in ASTM standard E112-13. A total of 131 single particles with radii between 3.8 and 20.7 μm were individually characterized magnetically to measure their transformation temperatures and the transformation behavior. Overall, the undercooling in each particle ranged from 11.3 to 59.4 K, with the smallest volumes having the largest magnitude and variance. The nucleation site potency distributions between the two domain sizes were statistically alike, suggesting that $L2_1$ domain size is not a critical factor in initiating nucleation at the length scales of this experiment. The implications for microlevel devices include opportunities to heat treat materials to high operational temperatures (e.g., 773 K) without impacting nucleation behavior.

I. INTRODUCTION

Thermoelastic martensitic transformations in shape memory alloys (SMAs) represent shear-dominated, diffusionless, and reversible processes between austenite and martensite phases [1,2]. According to classical martensitic nucleation theory, the martensitic nuclei form heterogeneously on preexisting and potent defect sites known as preembryos [2]. Experimental or computational studies employing techniques such as electron microscopy or molecular dynamics have attempted to provide insights into these preembryos by showing martensitic domains forming autocatalytically, after the initial nucleation, on dislocation types [3,4], twin boundaries [5], stacking faults [5], grain boundaries [6], vacancies [7,8], helium bubbles/voids [7], and antisite boundaries [8–10]. However, the preexisting defects primarily responsible for initiating martensitic nucleation and their potency remain unresolved due to the time and volume scale involved [11]. At the small length scales, where the probability of finding a potent defect is low, identifying and introducing potent defects could address nucleation limitations. As a result, martensitic nuclei could form with minimal undercooling and thus enhance operational efficiency and energy conversion across different length scales.

The importance of understanding defect potency in martensitic transformations extends beyond alloys to ceramics [12], polymers [13,14], and biological organisms [15,16] due to the shape memory effect (SME) and other multifunctional properties driven by martensitic transformations occurring in various material classes. Many SME materials are employed as nano- or microsized actuators, sensors, and energy harvesters. If engineered for low thermal hysteresis values, these devices could play an essential role in several emergent applications and miniaturization trends. For example, recent small-scale applications have included polydimethysiloxane - acrylonitrile butadiene styrene (PDMS-ABS) nitinol wires as bending microactuators with high actuation speeds [17], VO_2 coils as torsional microactuators with high power densities and rotational speeds [18], Ni-Ti films as microcooling devices [19], and Ni-Co-Mn-In magnetic particles as crack detection microsensors with tailorable thermal hysteresis [20,21].

Regardless of their application, the transition behavior of multifunctional alloys must be optimized to improve material performance in both bulk- and small-scale devices. Large thermal hysteresis widths impact martensitic transformations across all length scales due to intrinsic and extrinsic factors in the nucleation and growth of the cooling and heating transformations. However, the cooling transformation tends to have a greater impact on thermal hysteresis [22]. This is due to the heating transformation benefiting from the presence of retained austenite, which therefore negates the need for nucleation of the austenite phase. Reducing the thermal hysteresis widths in SMAs is vital to improving fatigue life [23,24] and thermodynamic efficiency [25–27]. At small scales, hysteresis scales with a reduction in volume following a power-law relationship creating the need for strategies to reduce hysteresis widths. For example, this need has been observed in polycrystalline Cu-Al-Ni microwires [28] and micropillars [29], which displayed increasing thermal and stress hysteresis at decreasing sizes. Additionally, Ni-Mn-Sn microfilms [30] and Ni-Co-Mn-Sn microparticles [31] displayed a power-law distribution showing increasing thermal hysteresis at decreasing volume.

The main factors affecting nucleation temperatures and thermal hysteresis differ in bulk scale from small-scale volumes. In bulk samples, tailoring thermal hysteresis strongly depends on chemical composition [32,33] and interfacial compatibility as calculated by cofactor conditions [34]. For example, large-volume thin films of Ni-Ti-Cu-V achieved near-zero thermal hysteresis by the combinatorial approach to composition variation [33], and large-volume thin films of $V_{1-x}W_xO_2$ achieved a 5 K hysteresis by the cofactor condition approach [35]. However, the cofactor conditions can also predict large functional reversibility and fatigue life in small-scale samples despite large thermal hysteresis widths [36].

In the case of small-scale samples, several size-dependent mechanisms are responsible for increasing thermal hysteresis by a power-law relationship, including

(1) an increase in internal friction arising from the interfacial obstacles, caused by the increase in surface area to volume ratio [37];

(2) changes in martensite and austenite free energy due to the contributions of interfacial energy terms [30]; and

(3) a probabilistic lack of active nucleation sites at smaller volumes concurrent with single-domain transformation behavior below a critical length $L < L_{cr}$ [2,11,31,38].

Based on the above three mechanisms, three regimes explain the rise of thermal hysteresis from bulk- to small-scale samples [30]. In the first regime, bulk materials have sufficient active nucleation sites to initiate the transformation. Chemical composition and phase compatibility are the leading factors for tuning hysteresis. In the second regime, the friction-induced regime, the facile motion of interfaces is limited by obstacles at the surface of samples as the relative surface area to volume ratio increases. Finally, the nucleation-limited regime ($L < L_{cr}$) occurs due to a lack of potent defects requiring larger driving forces to overcome the activation barrier associated with the nucleation of martensite domains. In each of these regimes, size effects at small scales are dependent on the quantity, type, and distribution of defects that can aid or impede nucleation formation and growth.

A closer look at the seminal work by Cech and Turnbull [39] is presented here to better understand the nucleation-limited regime. Their Fe-Ni small-particle experiments with diameters 30–90 μm characterized irreversible martensitic nucleation using a quantitative approach. The work found that nucleation begins on sparse heterogeneous sites. The analytical models presented in this work revealed that smaller particles require larger degrees of undercooling to initiate. Olson *et al.* [11] extended this work to formulate nucleation site potency distributions of the small-particle experiments using a probabilistic nucleation model. The result led to calculations of nucleation site densities versus thermodynamic driving force. This effort concluded that heterogeneous martensitic nucleation occurs in preexisting embryos and that sparse nucleation sites drive the transformation in bulk materials. This technique utilized a probabilistic Poisson-like distribution of defects, which treats nucleation as independent, uncorrelated, and random. As a result, the probability of an active site existing at smaller volumes decreases rapidly, leading to poor nucleation potency in small volumes.
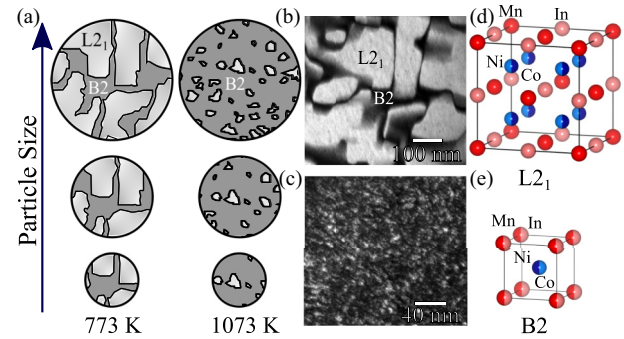

FIG. 1. (a) Two sets of $Ni_{45}Co_5Mn_{36.7}In_{13.3}$ microparticles with varying sizes and heat treatments were used to assess the nucleation potency of $L2_1$ domain interfaces. (b), (c) TEM images, adapted from Bruno *et al.* [9], demonstrate the extent of secondary annealing (773 K) to increase the $L2_1$ domain size. (d), (e) Changes to the structure are attributed to the order-disorder transformation.

Since the mid-1980s, several efforts have provided additional insights into how defects impact nucleation at small length scales. For example, Ni-Mn-Ga-Co films experienced low thermal hysteresis after repeated cycling attributed to defect formation [40]. However, thermal hysteresis remained high at even smaller volumes of 1.6 μm thickness. Transmission electron microscopy (TEM) images could not detect which defects were potent but elucidated mesoscopic phenomena in the absence of any microstructural differences between larger and smaller samples. Furthermore, Cu-Al-Ni pillars less than 2 μm showed abrupt and discontinuous transitions reminiscent of a nucleation-limited regime with increasing hysteresis at smaller volumes [41,42]. In another example, Ni-Fe-Ga pillars less than 10 μm showed decreasing martensite start temperatures (M_s) at smaller scales [43]. At even smaller length scales, a total lack of active nucleation sites suppressed the martensitic nucleation of nanometer NiTi films [44,45]. However, interfacial energies and strain effects by the substrate interface can also suppress thin films.

In this study, our main objective was to clarify the potential role of $L2_1$ domain interfaces as potent nucleation sites by comparing the undercooling of two sets of microparticles of $Ni_{45}Co_5Mn_{36.7}In_{13.3}$ subject to different heat treatments. Prior studies have investigated the significance of defects formed during the order-disorder transitions (e.g., long-range ordering, vacancies, and antisite defects) on the martensitic transformations in bulk-scale samples [9,21,46]. Many of these studies focus on bulk-scale phenomena that increase martensitic start temperatures due to autocatalytic defects instead of the preexisting defect distribution. To gain a more in-depth understanding of martensitic nucleation, we investigated different particle sizes at two different heat treatments using secondary annealing at 773 K to increase the size of the $L2_1$ domains and the associated interfacial area density by a factor of 5, from 60 to 300 μm^{-1} (Fig. 1) [9,21]. To assess the nucleation potency of the domain interfaces, we quantified the size effects of particle sizes (3.8 < r < 20.7 μm) using temperature-dependent magnetization curves. We demonstrated that the nucleation site potency distributions suggest that defects associated with the $L2_1$ domain interfacial area density are not critical in initiating nucleation.

However, high operational temperatures, indicated by secondary annealing temperatures of 773 K, may retain the transformation behavior for microlevel devices by maintaining consistent transformation widths and magnitudes.

II. METHODS

A. Materials

As-received $Ni_{45}Co_5Mn_{36.7}In_{13.3}$ (at. %) spherical particles were fabricated by gas atomization at radii $\leqslant 63$ μm. The particle composition was confirmed using wavelength dispersive x-ray spectroscopy (WDS) [21]. Heat treatment consisted of solution heat treatment (SHT) by sealing atomized particles in a quartz tube under an argon atmosphere (purity 99.999%) at 1073 K for 24 h, followed by a water quench. The second set of particles underwent homogenization followed by secondary annealing (SA) at 773 K for 3 h, followed by water quenching. No change in the reported chemical composition is expected due to the heat treatments, as shown in previously reported literature where samples ranging from 13.3 to 13.7 in indium content saw no change in the composition using WDS and *in situ* x-ray diffraction [46].

B. Characterization

The heat-treated particles were sieved into nine groups of 0–10, 10–15, 15–20, 20–25, 25–32, 32–38, 38–45, 45–52, and 52–63 μm diameters using a vibratory sieve shaker. To measure the thermophysical properties of the sieved groups, a TA Instruments Q2000 differential scanning calorimeter characterized each group at 10 K min^{-1}. Then, from the sieved groups, single particles were mounted onto 3×3 mm polyimide tape and stored in glass vials.

An optical microscope under reflective mode measured the particle diameters and confirmed that only one particle was mounted per tape. We utilized the diameter of the particles to determine size effects and to calculate their mass using the theoretical and experimental values [47] of 8.0 ± 0.05 g cm^{-3}. In total, 131 individual particles on a polyimide tape (N_{total}) were characterized. Of these, 63 were solution heat-treated particles, and 68 were secondary annealed. Particle sizes ranged from 3.8 to 20.7 μm in radius.

The magnetic moment of individual particles was measured using a Quantum Design magnetic property measurement system superconducting quantum interference device (SQUID) under the vibrating sample magnetometer mode, offering a sensitivity of less than 8×10^{-8} emu at magnetic fields larger than 2.5 kOe. Temperature sweeps were conducted at 5 K min^{-1} and a constant applied magnetic field of 5 kOe, sufficient to achieve saturation magnetization. Samples were heated up first to the austenite phase and followed by temperature cycling. Similarly, magnetic field sweeps were conducted at 3 kOe min^{-1} for the austenite phase at 360 K and the martensite phase at 220 K.

The microparticles were categorized as gradual (i.e., smooth), abrupt (i.e., sharp onset), or hybrid (i.e., a combination), depending on their heating/cooling transformation behavior. In gradual, abrupt, and hybrid transformations, the change in the magnetic moment (ΔM) was measured by forming tangent lines at the fully austenite (T_{aus}) and
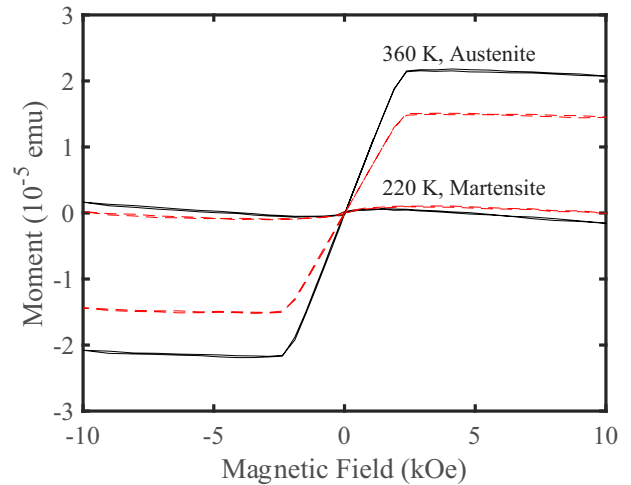

FIG. 2. Magnetic field sweeps $M(H)$ at constant temperatures (isothermal magnetization curves). The black solid curve is a solution heat-treated particle with a 37.0 ± 0.5 μm diameter. The red dashed curve is a secondary annealed particle with a 41.4 ± 0.5 μm diameter.

martensite (T_{mar}) portions of the signal. These lines were used to construct a midway (T_{midway}) line measured by $T_{midway} = (T_{aus} + T_{mar})/2$. A horizontal line representing thermal hysteresis was constructed at the intersections of the midway line with the signal, as shown in Fig. 4 by the gray line. Then a perpendicular line to the thermal hysteresis was constructed to measure the moment. The change in the magnetic moment was defined at the intersection with T_{aus} and T_{mar}. On the other hand, for abrupt and hybrid particles, the nucleation start temperature and the austenite finish temperature were measured at the discontinuity drops that accounted for at least 10% of the total signal response. Therefore, for the abrupt and hybrid transformations, the degree of undercooling was measured by $\Delta T_{cr} = A_f - M_s$.

III. RESULTS

A. Magnetic behavior of heat-treated alloy particles

The alloy $Ni_{45}Co_5Mn_{36.7}In_{13.3}$ (NiCoMnIn) was selected for its ease of changing transition temperature at the bulk scale using heat treatments and for its low thermal hysteresis near room temperature. The NiCoMnIn microparticles employed in this study are soft ferromagnets in the high-temperature austenite phase (Fig. 2) and paramagnetic in the low-temperature martensite phase, resulting in a temperature- and magnetic-field-induced shape memory effect also known as the metamagnetic shape memory effect [48]. Its parent structure is the $Ni_{50}Mn_{50-y}X_y$ ($X = $ In, Sn, Sb) family [49], a Ga-free Heusler-based ferromagnetic shape memory alloy. Cobalt was added to form the NiCoMnIn alloy to achieve a higher Curie temperature, magnetic saturation, Zeeman energy, and a near room temperature transformation [50,51]. Our group previously studied the $Ni_{43}Co_7Mn_{39}Sn_{11}$ alloy in the NiMnX family to explore SQUID magnetometry and the magnetic behavior of microparticles to formulate nucleation site potency distributions in thermoelastic martensitic transformations [31]. In this study, we extend our knowledge

of the NiMnX family of Heusler alloys to explore the role of heat treatments and order-disorder defects to nucleate martensitic phases.

We describe austenitic and martensitic phases depicted in Fig. 2 by their coupled magnetic and structural transitions and focus on their long-range order-disorder as the primary distinction between the two particle groups of this study (SHT and SA groups). The magnetic field sweep of Fig. 2 reveals a magnetic saturation near 2.5 kOe. This implies that temperature-dependent magnetization should be performed at constant applied magnetic fields higher than 2.5 kOe to maximize magnetic moments.

The high-temperature austenite phase is a ferromagnetic high-symmetry cubic $L2_1$ structure ($Fm\bar{3}m$ space group) [9,46,52], which exhibits ordering on the Mn/In sublattices. However, a small fraction of any sample has a combination of $L2_1$ with the $B2$ phase ($Pm\bar{3}m$), which exhibits disorder among the Mn/In and Ni/Co sublattices [9,21]. As shown in Fig. 1, the size of the $L2_1$ domains can be tailored by secondary annealing at 773 K for 3 h, increasing the domain size from 3.2 to 54.2 nm (measurement shown in Supplemental Material Fig. S1 [53]), as shown by the TEM micrographs using selected area electron diffraction microscopy. Using ASTM standards E112-13 and E562-19, we measured the interfacial area densities of 590.6 μm^{-1} for SHT and 50.6 μm^{-1} for SA (Fig. S1 [53]), which serve as sources for defects. Atomic-level defects such as antisites and vacancies can form at the interfaces of the $L2_1$ domains and function as potential nucleation sites for the paramagnetic martensitic phase.

The martensitic paramagnetic structure has a lower symmetry, treated as a Bain distortion from the $L2_1$ cubic phase, and is a body-centered tetragonal structure ($I4/mmm$ space group) [9,46,52]. Similarly, the $B2$ phase transforms to the paramagnetic and martensitic $P4/mmm$ space group. Additionally, martensitic structures can be modulated using a wave vector and referred to as 6M, 10M, 14M, or NM (nonmodulated) phases due to metastability from adaptive nano twins or from atomic shuffling [54–56].

The magnetic behavior of each particle was also measured under heating and cooling using the SQUID at a constant applied field of 5 kOe, which is above the saturation level seen in Fig. 2. In general, as the particle size decreases, the change in moment also decreases, as total magnetization is proportional to the volume of material present (Fig. 3). We also expect this behavior to hold in the length scales of this experiment. Large deviations from this relationship can suggest significant fractions of retained austenite and untransformed regions. Because we use the change in a magnetic moment as a proxy for phase fraction transformed, we validated our use of magnetization curves by establishing a relationship between the change in moment as a function of particle radius (Fig. 3). For the gradual, abrupt, and hybrid transformations a relationship was obtained using an empirical relationship, $\log(\Delta M) = 3\log(r) + b$, which linearizes the correlation between the moment, $\Delta M = M_{\text{aus}} - M_{\text{mar}}$ and the particle volume, $V = (4/3)\pi r^3$.

The change in the magnetic moment for both the SHT and SA particles correlated well with the calculated magnetic moment from bulk magnetization values, indicating near-complete transformation and thereby supporting the
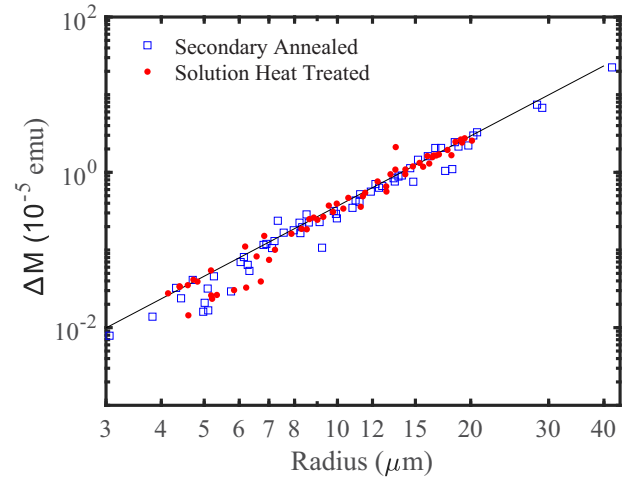

FIG. 3. Difference in magnetization versus particle size (radius) for gradual, abrupt, and hybrid particles. SA-treated particles are shown as blue squares and SHT as red circles. The solid black line represents an ideal scenario using the slope of an SHT particle of radii $19.0 \pm 0.5\,\mu$m (230 ng).

claim that magnetization is a good proxy for the extent of phase transformation (Fig. 3). The largest deviation observed in the model corresponded to smaller particle sizes and arose from noise, limitations of the measurement system, and some possible incompleteness in the transformation. Any degree of incomplete transformation is similar in both sample sets, and overall does not contribute to changes in martensitic nucleation between the two heat treatments. Therefore, the extent of total transformation in the particles is the same in both heat treatments, and neither treatment changes the range of magnetization observed (0.008 to 22.5 × 10^{-5} emu ± 6.1 × 10^{-8} emu; Fig. S2 [53]).

B. Phase transformation behavior of individual particles

By measuring the transition temperatures, the undercooling of individual spherical particles was characterized using magnetization curves under an applied temperature field $\Delta M(T)$. The temperature sweeps revealed abrupt, hybrid, and gradual transformations in the single-particle measurement (Fig. 4). Abrupt transformations occur when a sharp drop occurs in the magnetization. This behavior is shown in the black curve in Fig. 4 in the particle of size 6.2 μm (radii) with an undercooling of 58.5 K. In this particle, the heating and cooling curves display a sharp discontinuity. However, the red and blue curves are only abrupt during cooling (hybrid transformations). Notably, the blue and red heating curves are not entirely smooth but have a multistep transition affected by interface friction or defect pinning.

A total of 131 particles of sizes 3.8–20.7 μm in radii were measured using a magnetometer (63 SHT and 68 SA particles). Of these, 58.6% of SHT particles and 46.9% of SA particles displayed an abrupt transformation in cooling but not in heating (Table I). A total of 20.7% of SHT particles had abrupt transformations in both cooling and heating, and 25% in SA particles.
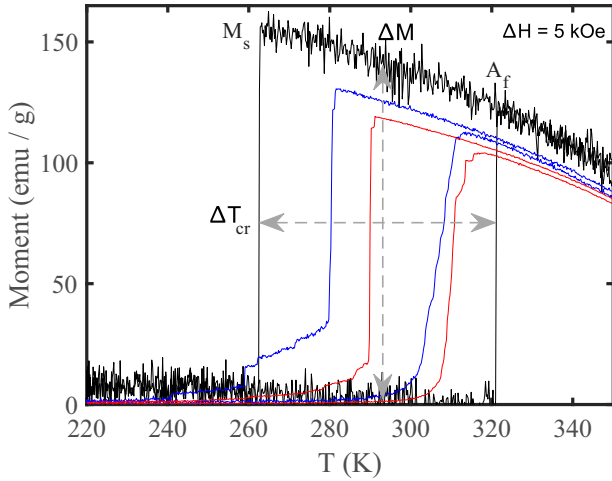
FIG. 4. Temperature sweeps $\Delta M(T)$ of single particles displaying a particle of $12.4 \pm 0.5\,\mu m$ in diameter (black, 8.0 ng), $26.4 \pm 0.51\,\mu m$ diameter (blue, 77.1 ng), and $38.0 \pm 0.5\,\mu m$ diameter (red, 230.0 ng). The black curve was displaced down by $30\,\mathrm{emu\,g^{-1}}$ for ease of comparison.

In literature, abrupt transformations are observed in bulk-size single crystals or oligocrystallines [57–59]. In our experiments, the microparticles are single crystals driven mostly by observable single-domain nucleation. When there are two or even three sharp jumps, this signifies the activation of additional nucleation domains within the particle or a disrupted multistep transformation. We can capture these sharp changes to the magnetic moment because of the sensitivity of the SQUID magnetometer (8×10^{-8} emu) and the nature of the small-particle experiment. As the probability of finding a potent defect decreases drastically at smaller volumes, the potent defects activated at higher driving forces eventually lead to distinguishable single interface motion.

Measuring the undercooling in nucleation-limited particles requires both the nucleation start temperature of the initial nuclei (i.e., taken at the onset of abruptness) and the equilibrium temperature. However, the equilibrium temperature of the martensitic transformation, T_{cr}, varies from one particle to another and is difficult to measure. Three models are presented in the literature for the determination of T_{cr} [57,60,61]: (1) frictionless transformations and therefore $T_{cr} > A_f$, (2) elastic accommodation and friction, $T_{cr} \approx A_f$, and (3) plastic accommodation and considerable friction, $T_{cr} \approx (M_s + A_f)/2$.

In the ideal scenario, if you consider a martensitic plate that forms as a single domain and grows abruptly, the transformation is frictionless, and T_{cr} is to the right of A_f. In this scenario, the plastic accommodation method would not be appropriate.

TABLE I. Fraction of SHT ($N_{total} = 63$) and SA particles ($N_{total} = 68$) that have abrupt, hybrid, or gradual transformations.

Transformation	SHT	SA
Abrupt	0.207	0.250
Hybrid	0.586	0.469
Gradual	0.207	0.281

However, for nucleation-limited and thermoelastic particles, a certain degree of friction is observed by multiple sharp drops in the magnetic moment and by an increase of interface friction due to an increasing surface area to volume. Therefore, the second model is best suited to measure undercooling as $\Delta T_{cr} = A_f - M_s$.

The transition temperatures of 96 abrupt and hybrid particles were quantified and analyzed to determine the nucleation potency of the $L2_1$ domain interface. An asymmetry was observed in the austenite to martensite transition temperatures [Fig. 5(a)]. At higher degrees of hysteresis, it is observed that the depression of the M_s temperature is primarily responsible for increasing thermal hysteresis rather than an increase in A_f. This is attributed to residual austenite found in between variants and confined spaces caused by martensite distortions and shear [22]. The retained austenite serves as preexisting nuclei for the heating transition. Additionally, from Fig. 5(b), we can see additional evidence of the asymmetry in the change between transition temperatures as particle size decreases. A greater number of martensitic start temperatures at smaller sizes trend towards lower values, and at the same time, lower M_s values are associated with greater undercooling.

In order to calculate nucleation site potency distributions, the chemical driving force as a function of particle volume was sampled to the smallest volume measurable by the instrumentation, revealing the extent of size effects. The sampling distribution displayed increasing undercooling as particle size decreased [Fig. 5(c)]. At the smallest of volumes, similar-sized particles had undercooling values near bulk levels (<15 K), and others with large values near 60 K ± 1.2 K (Fig. S2 [53]). This suggests that at volumes less than $5000\,\mu m^3$, some particles contained highly potent nucleation sites, whereas others were starved of defects. On the other hand, at even larger volumes, the variance in the undercooling values is expected to decrease until bulk levels are reached.

The observations of the undercooling size effects shown in Fig. 5(c) display a trend from the bulk regime to the friction-induced regime and to the nucleation-limited regime. The bulk level places a floor or limitation on the minimum hysteresis achievable. Thereby, none of the particles show an undercooling of less than 10 K. This is attributed to bulk samples already having the highest potent defect present. As the volume decreases, the required driving force for nucleation increases due to surface interface motion at larger surface-to-volume ratios in the friction-induced regime. Then, at around 24–28 μm in diameter, the undercooling climbs steeply as the particles enter a regime limited by an even lower probability of finding a potent defect (i.e., starvation of defects). At smaller sizes, martensitic suppression is known to occur in the absolute absence of sufficiently active nucleation sites [62].

IV. DISCUSSION

A. Nucleation-limited particles and nucleation potency

Statistical nucleation analysis aims to understand the role of some processing variable or structural descriptor on the density of active nucleation sites (sites cm^{-3}) by quantifying nucleation statistics in populations of particles of different volumes. In principle, particle volume could vary broadly and
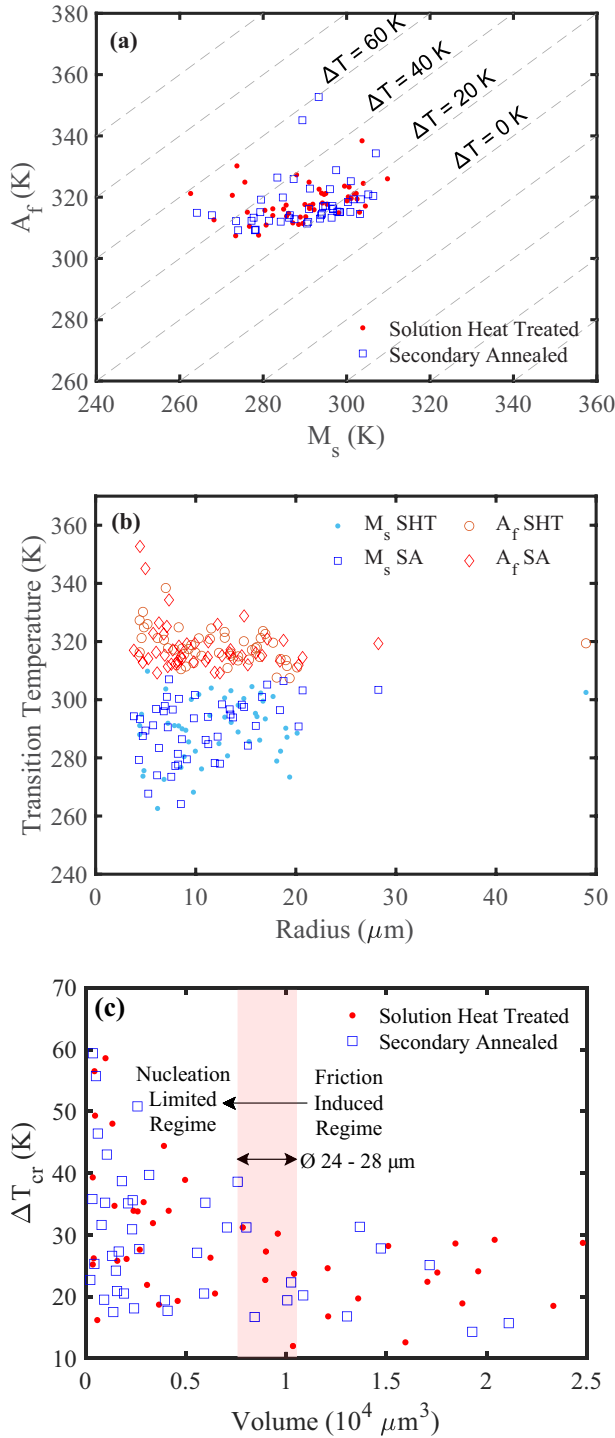
FIG. 5. Abrupt and hybrid transformation behavior. (a) A_f temperature for SHT (red circles) and SA (blue squares). (b) Transition temperature for SA (A_f red diamonds and M_s blue squares) and SHT (A_f orange open circles and M_s light-blue circles). (c) Undercooling for SHT (red circles) and SA (blue squares). The red band indicates the critical size of the transition to the nucleation-limited regime.

is restricted only by the sensitivity of the technique used to observe the nucleation phenomena. In this study, abrupt and hybrid transformations were used to measure M_s temperatures required to assess the nucleation potency of order-disorder interfaces.
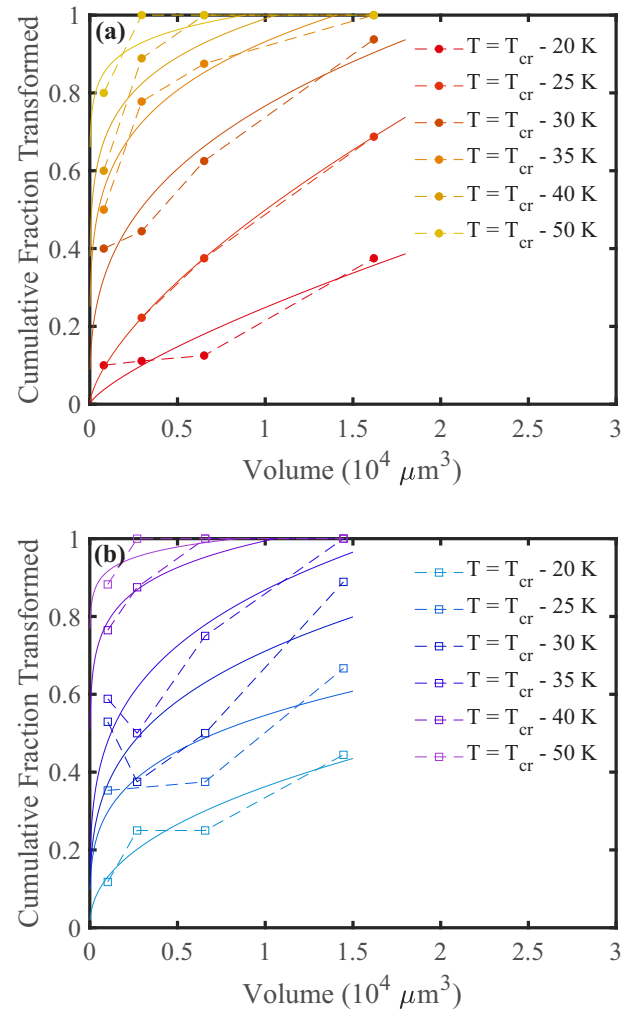

FIG. 6. Martensite cumulative fraction transformed as a function of volume at different driving forces. (a) The solution heat-treated set (solid circles). (b) The secondary annealing set (open squares).

To measure the nucleation site potency distribution, we adopt, based on a Poisson-like distribution of nucleation loci per particle, the probability (P) such that at a given volume, at least one active nucleation site exists [11]:

$$P = 1 - e^{-V\rho(\Delta G)}, \qquad (1)$$

where P is the cumulative percentage of particles transformed, V is the particle volume, ρ is the density of the active nucleation site as a function of ΔG, and ΔG is the molar Gibbs free energy change.

We measure the cumulative number of particles that have transformed at a given size bin and temperature bin taken from the data in Fig. 5(c). A set of temperature bins is derived from the intervals of $\Delta T_{cr} = 20, 25, 30, 35, 40,$ and 50 (K). For the size bins, four intervals are used: volume = 2, 4, 9, and 25 ($10^3 \, \mu m^3$). The binning from the selected intervals was used to calculate the cumulative probability distributions (Fig. 6). At each cumulative fraction transformed curve, the probability function [Eq. (1)] is fitted to determine the nucleation site potency (ρ) governing that driving force. Furthermore, the following power-law function is fitted to the calculated potencies
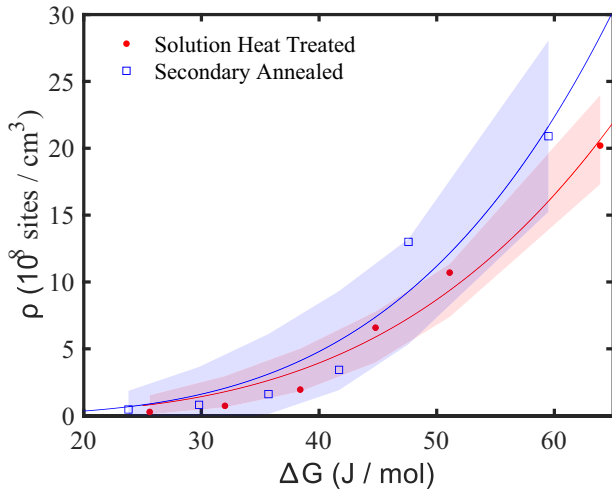
FIG. 7. Nucleation site potency distributions of solution heat-treated in red and secondary annealed in blue using a 95% confidence interval.

(Fig. 7):

$$\rho = \alpha \Delta G^{\beta}, \qquad (2)$$

where ρ is the density of nucleation sites, α is a proportionality constant, ΔG is the nucleation barrier, and β is the fitting exponent. To measure the chemical driving force, $\Delta G = \Delta S$ $(T_{cr} - T)$, we use the temperature interval $(T_{cr} - T)$ associated with the calculated potency and the entropy change of fusion (19.7 for SHT and 18.37 J kg^{-1} K^{-1} for SA) measured by calorimetry of a sample of particles within the sizes of 53–75 μm in diameter.

The power-law function [Eq. (2)] for the two sets of samples displayed a goodness of fit of $R^2 = 0.98$ (SHT) and 0.94 (SA). According to this relation, both potency curves have similar fitting exponents (β) at 5.0 and 4.5 (Fig. 7). The solution heat-treated potency curve (Fig. 7) is given by $\rho_{SHT} = 3.0 \times 10^{-8} (\Delta G^{5.0})$ in (sites cm^{-3}). On the other hand, the secondary annealed curve is given by $\rho_{SA} = 2.2 \times 10^{-7} (\Delta G^{4.5})$.

The extremes in large and small undercooling observed in the measurement of transformation behavior (Fig. 5) is due to the higher probability of more potent defects occurring in the large particles due to their size and the relatively small probability of these defects occurring in smaller particles. In the smallest volumes, the sparseness of the most potent defect is greater, resulting in a greater thermochemical driving force required to activate nucleation from less-potent defects. Even at small chemical driving forces, the concentration of nucleation sites (approximately 1×10^8 sites cm^{-3}) is one order of magnitude greater than the Fe-Ni particles studied by Olson *et al.*, which were investigated at much larger driving forces [11]. However, it represents a similar potency distribution to Ni-Co-Mn-Sn [31] particles. The subsequent magnitude of the potency distribution (Fig. 7) depends on the smallest volume measured based on the available defect potencies, the distribution of sample sizes considered in the study, and instrumentation capability. Overall, the nucleation site density power law depends on the range of relevant sample sizes

measured and the underlying Poisson-like defect distribution that leads to the sampling distribution of nucleation events [Fig. 5(c)].

Ultimately, based on Fig. 7, the potency distribution between the two heat treatment conditions was statistically equivalent. This conclusion considers the margin of error using a 95% confidence interval that overlaps the two data sets. Therefore, the $L2_1$ interface and corresponding antisite boundaries and defects do not represent potent nucleation sites for the initial formation of nucleation domains. While structural defects at the interface may be sufficient to nucleate under some large chemical driving force, there exist other preexisting defect states that are different from the defects associated with $L2_1$ domains which are more potent. This observation can be extended to any defect formed by the interface, as well as any changes in concentration change or lattice mismatches by the $L2_1$ or $B2$ domains which do not serve as potent nucleation sites. Importantly, a potential study in the future can further investigate other impacts induced by the interface strain on the thermoelastic properties of Ni-Co-Mn-In and related alloys.

Despite this observation, order-disorder defects are known to tailor thermal hysteresis at larger length scales [21], suggesting that their principal role is in affecting the motion of grain boundaries during the phase transformation. For example, the thermomagnetic characterization of bulk and agglomerated particles (25–63 μm in diameter) showed a reduction in thermal hysteresis after secondary annealing near 773 K [21]. Therefore, secondary annealing is an effective strategy to tailor the thermal hysteresis of samples at the bulk scale and the friction-induced length scales (average diameter of 44 μm, assuming a Gaussian distribution). Molecular dynamics studies in stress-induced NiTi [8,63] may support the idea that antisite defects neither promote the nucleation start temperature (preexisting distribution) nor cause a large inhibition of the martensitic transformation. A random distribution of antisite defect was attributed to having least martensitic suppression caused by boundary motion pinning compared to vacancies, interstitials, and vacancy clusters. This outcome was attributed to antisite defects having the smallest stress distortion fields when compared to the other defects. However, molecular dynamic studies of thermally induced Ni-Al showed that martensitic nucleation can initiate by larger and more complex defects such as dislocation dipoles [4]. The stress field surrounding the dislocation dipole was found to contribute to the lattice distortion required to form martensitic domains.

When comparing within the NiCoMnX family, the potency curves of NiCoMnIn for both heat treatments are shifted slightly to the right of the Ni$_{43}$Co$_7$Mn$_{39}$Sn$_{11}$, implying that it takes a larger chemical driving force in NiCoMnIn to excite an equivalent density of nucleation sites as in Ni$_{43}$Co$_7$Mn$_{39}$Sn$_{11}$ (Fig. 8). This correlates with the lower thermal hysteresis in bulk Ni$_{43}$Co$_7$Mn$_{39}$Sn$_{11}$ approximately 8 K) compared to Ni$_{45}$Co$_5$Mn$_{36.7}$In$_{13.3}$ (approximately 12 K), thus requiring lower driving forces even at the bulk scale. Furthermore, microparticles of VO$_2$ [64] ($V < 28.0 \, \mu$m^3) and nanoparticles of VO$_2$ [65], along with the NiCoMnX family, lie to the left of the < 20 K boundary line, while Al$_2$O$_3$ + ZrO$_2$, Ni-Al, and Fe-Ni lie to the right. This boundary separates thermoelastic
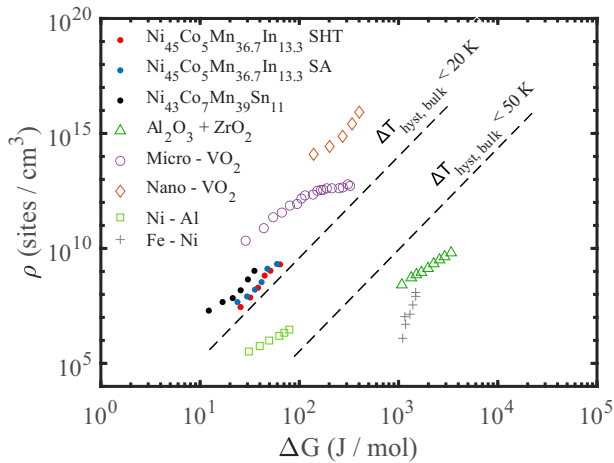
FIG. 8. Nucleation site potency distributions compared to several other material classes, including $Ni_{43}Co_7Mn_{39}Sn_{11}$ [31], VO_2 [64,65], NiAl [66], FeNi [11,39], and $Al_2O_3 + ZrO_2$ [67], adapted from [31].

transformations that require lower energies for nucleation from those material systems that display larger thermal hysteresis values at the bulk scales or irreversible transformations.

V. CONCLUSIONS

This study contributes to our understanding of nucleation potencies in reversible thermoelastic transformations impacted by heat treatments, order-disorder interface defects, and the relative sizes at which samples transition to the nucleation-limited regime. Here, SQUID magnetometry is employed as a high-fidelity technique to quantify nucleation site potency distributions and we experimentally consider order-disorder interfaces as potential preexisting defects. We concluded that the variation in $L2_1$ domain interfacial density at the length scales observed did not contribute to an increase in martensitic potency across the length scales. However,

we discovered that postprocessing at secondary annealing (773 K) for 3 h represented an insensitivity of nucleation rate to order-disorder interfaces in NiCoMnIn particles.

Additionally, we made several key observations about the transformation behavior of alloy particles and how it relates to the potency distributions. Based on Figs. 4 and 5, the particles under study were nucleation limited on cooling due to starvation of defects at smaller sizes, measured in this study by abrupt transformations characteristic of single-domain transformations. We also observed that at radii below 12–14 μm, a transition from the friction-induced regime to the nucleation-limited regime occurred ($L < L_{cr}$) [Fig. 5(c)]. However, the attributes of the sampling distributions making up the nucleation potency curves need to be measured case by case due to the current difficulty in computationally predicting the preexisting defect state unique to each material class and various processing techniques.

We also observed particles below 10 μm radii with near to bulk hysteresis, indicating that even in the smallest of volumes, stable high-potency nucleation sites can exist, suggesting the plausibility of intentionally introducing potent defects to small volumes of shape memory alloys, with the goal of improving energy conversion and fatigue life in SME-based nano- and microscale devices. In contrast, similar small sizes with the largest undercooling near 60 K are good candidates for a different type of application requiring large energy damping or metastable "latching" type behavior. The future directions in this research should investigate additional defect sizes, types, and potencies that may serve as potent nucleation sites in nucleation-limited thermoelastic martensitic transformations.

[1] K. Bhattacharya, S. Conti, G. Zanzotto, and J. Zimmer, Crystal symmetry and the reversibility of martensitic transformations, Nature (London) **428**, 55 (2004).

[2] G. B. Olson and M. Cohen, A perspective on martensitic nucleation, Annu. Rev. Mater. Sci. **11**, 1 (1981).

[3] A. Ibarra, D. Caillard, J. San Juan, and M. L. Nó, Martensite nucleation on dislocations in Cu–Al–Ni shape memory alloys, Appl. Phys. Lett. **90**, 101907 (2007).

[4] B. Li, X. M. Zhang, P. C. Clapp, and J. A. Rifkin, Molecular dynamics simulations of the effects of defects on martensite nucleation, J. Appl. Phys. **95**, 1698 (2004).

[5] G. B. Olson and M. Cohen, Kinetics of strain-induced martensitic nucleation, Metall. Trans. A **6**, 791 (1975).

[6] T. Song and B. C. De Cooman, Martensite nucleation at grain boundaries containing intrinsic grain boundary dislocations, ISIJ Int. **54**, 2394 (2014).

[7] C. Yang, Y. Pachaury, A. El-Azab, and J. Wharry, Molecular dynamics simulation of vacancy and void effects on strain-induced martensitic transformations in Fe-50 at.% Ni model concentrated solid solution alloy, Scr. Mater. **209**, 114394 (2022).

[8] C. Yang and J. P. Wharry, Role of point defects in stress-induced martensite transformations in NiTi shape memory alloys: A molecular dynamics study, Phys. Rev. B **105**, 144108 (2022).

[9] N. M. Bruno, D. Salas, S. Wang, I. V. Roshchin, R. Santamarta, R. Arroyave, T. Duong, Y. I. Chumlyakov, and I. Karaman, On the microstructural origins of martensitic transformation arrest in a NiCoMnIn magnetic shape memory alloy, Acta Mater. **142**, 95 (2018).

[10] D. Wang, D. Lv, Y. Gao, Y. Wang, X. Ren, and Y. Wang, Defect strength and strain glass state in ferroelastic systems, J. Alloys Compd. **661**, 100 (2016).

[11] G. B. Olson, K. Tsuzaki, and M. Cohen, Statistical aspects of martensitic nucleation, MRS Online Proc. Libr. **57**, 129 (1985).

[12] A. Lai, Z. Du, C. L. Gan, and C. A. Schuh, Shape memory and superelastic ceramics at small scales, Science **341**, 1505 (2013).

[13] C. A. Spiegel, M. Hackner, V. P. Bothe, J. P. Spatz, and E. Blasco, 4D printing of shape memory polymers: from macro to micro, Adv. Funct. Mater. **32**, 2110580 (2022).

[14] M. Zare, P. Davoodi, and S. Ramakrishna, Electrospun shape memory polymer micro-/nanofibers and tailoring their roles for biomedical applications, Nanomaterials **11**, 933 (2021).

[15] C. P. Frick, T. W. Lang, K. Spark, and K. Gall, Stress-induced martensitic transformations and shape memory at nanometer scales, Acta Mater. **54**, 2223 (2006).

[16] W. Falk and R. D. James, Elasticity theory for self-assembled protein lattices with application to the martensitic phase transition in bacteriophage T4 tail sheath, Phys. Rev. E **73**, 011917 (2006).

[17] S.-H. Song, J.-Y. Lee, H. Rodrigue, I.-S. Choi, Y. J. Kang, and S.-H. Ahn, 35 Hz shape memory alloy actuator with bending-twisting mode, Sci. Rep. **6**, 21118 (2016).

[18] K. Liu, C. Cheng, J. Suh, R. Tang-Kong, D. Fu, S. Lee, J. Zhou, L. O. Chua, and J. Wu, Powerful, multifunctional torsional micromuscles activated by phase transition, Adv. Mater. **26**, 1746 (2014).

[19] H. Ossmer, C. Chluba, S. Kauffmann-Weiss, E. Quandt, and M. Kohl, TiNi-based films for elastocaloric microcooling—Fatigue life and device performance, APL Mater. **4**, 064102 (2016).

[20] N. E. Barta and I. Karaman, Embedded magnetic shape memory sensory particles in lightweight composites for crack detection, Mater. Sci. Eng., A **751**, 201 (2019).

[21] W. Cho, D. Salas, N. Barta, and I. Karaman, Engineering thermal hysteresis of ferromagnetic shape memory alloy sensory particles, Scr. Mater. **213**, 114619 (2022).

[22] A. Diestel, R. Niemann, B. Schleicher, K. Nielsch, and S. Fähler, Reducing hysteresis losses by heating minor loops in magnetocaloric Ni–Mn–Ga–Co films, Energy Technol. **6**, 1463 (2018).

[23] K. Gall and H. J. Maier, Cyclic deformation mechanisms in precipitated NiTi shape memory alloys, Acta Mater. **50**, 4643 (2002).

[24] Z. Moumni, A. V. Herpen, and P. Riberty, Fatigue analysis of shape memory alloys: Energy approach, Smart Mater. Struct. **14**, S287 (2005).

[25] P. J. Shamberger and F. S. Ohuchi, Hysteresis of the martensitic phase transition in magnetocaloric-effect Ni-Mn-Sn alloys, Phys. Rev. B **79**, 144407 (2009).

[26] S. Fähler, U. K. Rößler, O. Kastner, J. Eckert, G. Eggeler, H. Emmerich, P. Entel, S. Müller, E. Quandt, and K. Albe, Caloric effects in ferroic materials: New concepts for cooling, Adv. Eng. Mater. **14**, 10 (2012).

[27] T. D. Brown, T. Buffington, and P. J. Shamberger, Effects of hysteresis and Brayton cycle constraints on magnetocaloric refrigerant performance, J. Appl. Phys. **123**, 185101 (2018).

[28] Y. Chen and C. A. Schuh, Size effects in shape memory alloy microwires, Acta Mater. **59**, 537 (2011).

[29] J. San Juan, M. L. Nó, and C. A. Schuh, Superelastic cycling of Cu–Al–Ni shape memory alloy micropillars, Acta Mater. **60**, 4093 (2012).

[30] Y. Zhang, J. Billman, and P. J. Shamberger, Size effects in the Martensitic transformation hysteresis in Ni–Mn–Sn Heusler alloy films, Acta Mater. **180**, 116 (2019).

[31] Y. Zhang, C. Lago, I. Karaman, and P. J. Shamberger, Nucleation site potency distributions in thermoelastic martensitic transformation in $Ni_{43}Co_7Mn_{39}Sn_{11}$ particles, Phys. Rev. Mater. **5**, 023401 (2021).

[32] M. Zarinejad and Y. Liu, Dependence of transformation temperatures of NiTi-based shape-memory alloys on the number and concentration of valence electrons, Adv. Funct. Mater. **18**, 2789 (2008).

[33] N. M. Al Hasan, H. Hou, S. Sarkar, S. Thienhaus, A. Mehta, A. Ludwig, and I. Takeuchi, Combinatorial synthesis and high-throughput characterization of microstructure and phase transformation in Ni–Ti–Cu–V quaternary thin-film library, Engineering **6**, 637 (2020).

[34] H. Gu, L. Bumke, C. Chluba, E. Quandt, and R. D. James, Phase engineering and supercompatibility of shape memory alloys, Mater. Today **21**, 265 (2018).

[35] Y. G. Liang, S. Lee, H. S. Yu, H. R. Zhang, Y. J. Liang, P. Y. Zavalij, X. Chen, R. D. James, L. A. Bendersky, A. V. Davydov *et al.*, Tuning the hysteresis of a metal-insulator transition via lattice compatibility, Nat. Commun. **11**, 1 (2020).

[36] X. Ni, J. R. Greer, K. Bhattacharya, R. D. James, and X. Chen, Exceptional resilience of small-scale $Au_{30}Cu_{25}Zn_{45}$ under cyclic stress-induced phase transformation, Nano Lett. **16**, 7621 (2016).

[37] S. M. Ueland and C. A. Schuh, Transition from many domain to single domain martensite morphology in small-scale shape memory alloys, Acta Mater. **61**, 5618 (2013).

[38] G. B. Olson, Advances in theory: Martensite by design, Mater. Sci. Eng., A **438-440**, 48 (2006).

[39] R. E. Cech and D. Turnbull, Heterogeneous nucleation of the martensite transformation, JOM **8**, 124 (1956).

[40] A. Diestel, P. Chekhonin, R. Niemann, W. Skrotzki, K. Nielsch, and S. Fähler, Reducing thermal hysteresis in epitaxial Ni–Mn–Ga–Co films by transformation cycling, Phys. Status Solidi B **255**, 1700330 (2018).

[41] J. San Juan and M. L. Nó, Superelasticity and shape memory at nano-dcale: Size effects on the martensitic transformation, J. Alloys Compd. **577**, S25 (2013).

[42] J. San Juan, M. L. Nó, and C. A. Schuh, Superelasticity and shape memory in micro- and nanometer-scale pillars, Adv. Mater. **20**, 272 (2008).

[43] N. Ozdemir, I. Karaman, N. A. Mara, Y. I. Chumlyakov, and H. E. Karaca, Size effects in the superelastic response of $Ni_{54}Fe_{19}Ga_{27}$ shape memory alloy pillars with a two stage martensitic transformation, Acta Mater. **60**, 5670 (2012).

[44] T. Waitz, V. Kazykhanov, and H. P. Karnthaler, Martensitic phase transformations in nanocrystalline NiTi studied by TEM, Acta Mater. **52**, 137 (2004).

[45] Y. Q. Fu, S. Zhang, M. J. Wu, W. M. Huang, H. J. Du, J. K. Luo, A. J. Flewitt, and W. I. Milne, On the lower thickness boundary of sputtered TiNi films for shape memory application, Thin Solid Films **515**, 80 (2006).

[46] D. Salas, Y. Wang, T. C. Duong, V. Attari, Y. Ren, Y. Chumlyakov, R. Arróyave, and I. Karaman, Competing interactions between mesoscale length-scales, order-disorder, and martensitic transformation in ferromagnetic shape memory alloys, Acta Mater. **206**, 116616 (2021).

[47] F. Puglielli, V. Mussi, F. Cugini, N. Sarzi Amadè, M. Solzi, C. Bennati, S. Fabbrici, and F. Albertini, Scale-up of magnetocaloric NiCoMnIn Heuslers by powder metallurgy for room temperature magnetic refrigeration, Front. Energy Res. **7**, 150 (2020).

[48] R. Kainuma, K. Oikawa, W. Ito, Y. Sutou, T. Kanomata, and K. Ishida, Metamagnetic shape memory effect in NiMn-based Heusler-type alloys, J. Mater. Chem. **18**, 1837 (2008).

[49] Y. Sutou, Y. Imano, N. Koeda, T. Omori, R. Kainuma, K. Ishida, and K. Oikawa, Magnetic and martensitic transformations of NiMnX (X = In, Sn, Sb) ferromagnetic shape memory alloys, Appl. Phys. Lett. **85**, 4358 (2004).

[50] R. Kainuma, Y. Imano, W. Ito, Y. Sutou, H. Morito, S. Okamoto, O. Kitakami, K. Oikawa, A. Fujita, and T. Kanomata, Magnetic-field-induced shape recovery by reverse phase transformation, Nature (London) **439**, 957 (2006).

[51] H. E. Karaca, I. Karaman, B. Basaran, Y. Ren, Y. I. Chumlyakov, and H. J. Maier, Magnetic field-induced phase transformation in NiMnCoIn magnetic shape-memory alloys— A new actuation mechanism with large work output, Adv. Funct. Mater. **19**, 983 (2009).

[52] D. Salas, O. Eliseeva, Y. Wang, T. Duong, Y. I. Chumlyakov, Y. Ren, R. Arroyave, and I. Karaman, Effects of composition and crystallographic ordering on the ferromagnetic transition in NiCoMnIn magnetic shape memory alloys, Acta Mater. **166**, 630 (2019).

[53] See Supplemental Material at http://link.aps.org/supplemental/10.1103/PhysRevMaterials.8.014411 for domain size, interfacial area density, and confidence interval calculations.

[54] S. Kaufmann, U. K. Rößler, O. Heczko, M. Wuttig, J. Buschbeck, L. Schultz, and S. Fähler, Adaptive modulations of martensites, Phys. Rev. Lett. **104**, 145702 (2010).

[55] A. Sozinov, D. Musiienko, A. Saren, P. Veřtát, L. Straka, O. Heczko, M. Zelený, R. Chulist, and K. Ullakko, Highly mobile twin boundaries in seven-layer modulated Ni–Mn–Ga–Fe martensite, Scr. Mater. **178**, 62 (2020).

[56] R. Chulist and P. Czaja, On the role of atomic shuffling in the 4O, 4M and 8M martensite structures in Ni-Mn-Sn single crystal, Scr. Mater. **189**, 106 (2020).

[57] R. J. Salzbrenner and M. Cohen, On the thermodynamics of thermoelastic martensitic transformations, Acta Metall. **27**, 739 (1979).

[58] G. B. Olson and M. Cohen, Reply to "On the equilibrium temperature in thermoelastic martensitic transformations," Scr. Metall. **11**, 345 (1977).

[59] S. M. Ueland, Y. Chen, and C. A. Schuh, Oligocrystalline shape memory alloys, Adv. Funct. Mater. **22**, 2094 (2012).

[60] J. Ortín and A. Planes, Thermodynamic analysis of thermal measurements in thermoelastic martensitic transformations, Acta Metall. **36**, 1873 (1988).

[61] G. B. Olson and M. Cohen, Thermoelastic behavior in martensitic transformations, Scr. Metall. **9**, 1247 (1975).

[62] T. Waitz, T. Antretter, F. D. Fischer, and H. P. Karnthaler, Size effects on martensitic phase transformations in nanocrystalline NiTi shape memory alloys, Mater. Sci. Technol. **24**, 934 (2008).

[63] A. Hinojos, D. Hong, H. Sriram, L. Feng, C. Yang, J. P. Wharry, X. Gao, K. Hattar, N. Li, J. E. Schaffer *et al.*, Taming the pseudoelastic response of nitinol using ion implantation, Scr. Mater. **226**, 115261 (2023).

[64] H. Clarke, B. D. Caraway, D. G. Sellers, E. J. Braham, S. Banerjee, R. Arróyave, and P. J. Shamberger, Nucleation-controlled hysteresis in unstrained hydrothermal VO_2 particles, Phys. Rev. Mater. **2**, 103402 (2018).

[65] R. Lopez, T. E. Haynes, L. A. Boatner, L. C. Feldman, and R. F. Haglund, Size effects in the structural phase transition of VO_2 nanoparticles, Phys. Rev. B **65**, 224113 (2002).

[66] S. Rubini, C. Dimitropoulos, and F. Borsa, NMR investigation of the martensitic transformation in fine particles of Ni-Al alloys, Phys. Rev. B **49**, 9331 (1994).

[67] A. H. Heuer, N. Claussen, W. M. Kriven, and M. Ruhle, Stability of tetragonal ZrO_2 particles in ceramic matrices, J. Am. Ceram. Soc. **65**, 642 (1982).